A&A 673, A106 (2023)
https://doi.org/10.1051/0004-6361/202244121

Astronomy & Astrophysics

Statistical study of the Jovian decametric radio emissions based on multiple-view observations from remote radio instruments

Ruobing Zheng[1,2], Yuming Wang[1,2,3], Xiaolei Li[1,2], Chuanbing Wang[1,2], and Xianzhe Jia[4]

[1] Deep Space Exploration Laboratory/School of Earth and Space Sciences, University of Science and Technology of China, Hefei 230026, PR China
e-mail: ymwang@ustc.edu.cn
[2] CAS Center for Excellence in Comparative Planetology/CAS Key Laboratory of Geospace Environment, University of Science and Technology of China, Hefei 230026, PR China
[3] Hefei National Laboratory, University of Science and Technology of China, Hefei, PR China
[4] Department of Climate and Space Sciences and Engineering, University of Michigan, Ann Arbor, MI 48109-2143, USA

Received 26 May 2022 / Accepted 8 March 2023

ABSTRACT

To better understand the physical processes associated with Jovian decametric (DAM) radio emissions, we present a statistical study of DAM emissions and inferred characteristics of DAM sources based on multiview observations from the Wind and STEREO spacecraft. Altogether, we analyze 81 isolated, strong events in radio dynamic spectra from 2008 to 2014. The apparent rotation speed of DAM events derived from multiple spacecraft observations can be used to distinguish Io-related and non-Io-related DAM emission. We find that the rotation speed of Io-DAM events is in the range of 0.15–0.6 Ω_J and that the rotation speed of non-Io DAM events is between 0.7–1.2 Ω_J. We find the occurrence probability of isolated, strong Io-DAM events to be about seven times that of isolated, strong non-Io DAM events. We locate the sources of 79 DAM events (including ten events observed by the Nançay Decameter Array) and infer their emission angles and associated electron energy. Our statistical results show that the DAM source locations (both Io and non-Io) are distributed in three preferred high-latitude regions, with two in the southern hemisphere (around 30° to 150° and around 270° to 330° in System III longitudes) and one in the northern hemisphere (around 150° to 210°), which is probably caused by the nonsymmetrical topology of Jupiter's magnetic field. The difference between the Io-DAM source footprints and the Io auroral UV spots changes with the Io position in System III longitude, which is consistent with previous results. In addition, for the same type of DAM events (e.g., type A or C), the emission angles of non-Io DAM events are smaller than those of Io-DAM events, and all the emission angles range from 60° to 85°. Correspondingly, the energy associated with the electrons responsible for exciting the radio emissions is estimated to range between 2 and 22 keV.

Key words. radiation mechanisms: non-thermal – methods: statistical – planets and satellites: aurorae – planets and satellites: individual: Jupiter

1. Introduction

Jupiter's radio emission has various components spanning from below 10 kHz to above 3 GHz. The auroral, high-latitude components are the most intensive, non-thermal radiation generated in the Jovian inner magnetosphere and upper ionosphere (Zarka 1998). Decametric (DAM) radio emission was first discovered by Burke & Franklin (1955). It has frequencies ranging from 1 MHz to 40 MHz (Zarka et al. 2001). The mechanism for generating the Jovian radio emission is Cyclotron Maser Instability (CMI), a theory commonly applied to understand planetary radio emissions (e.g., Wu & Lee 1979; Zarka 1998; Huff et al. 1988; Kurth et al. 2005; Treumann 2006), and the loss-cone electron distribution has been recently shown by Juno in situ observations to be responsible for driving the CMI (e.g., Louarn et al. 2017, 2018). Based on the loss-cone driven CMI theory, Hess et al. (2008, 2010) established an emission angle function related to active electron energy and the Jovian magnetic field. This function has become the core of several methods, including the ExPRES (Exoplanetary and Planetary Radio Emission Simulator; see Louis et al., 2019) and the method developed by Wang et al. (2020) to infer the source location and characteristics of DAM emissions.

Abundant observations together with the CMI theory suggest that DAM emission radiates along a hollow emission cone with a narrow cone wall. The emission half angle is between 60°–90° (Queinnec & Zarka 1998; Hess et al. 2008, 2014), and the thickness of the cone wall is about 1°–2° (Kaiser et al. 2000; Panchenko & Rucker 2016). Based on the CMI theory and the refraction effect in the source region, the emission angle varies with the radiation frequency, and the DAM emission appears in an arc shape in the time-frequency spectrum with the shape lasting from minutes to hours (Carr et al. 1983; Zarka 1998; Hess et al. 2008). As viewed by a day-side observer, the dawn-side emission has a vertex-early (VE) arc shape, and the dusk-side emission is vertex-late (VL) due to the geometry of the emission cone. The dominant emission from the northern hemisphere is right-hand polarized, while the dominant emission in the southern hemisphere is left-hand polarized, due to the angle between the radiation wave vector and the direction of Jupiter's magnetic field. Based on these characteristics of the DAM emission (i.e., its arc shape in the spectrum and the polarization of the wave), the source region of DAM emissions can be classified into four regions: the northeastern quadrant (A), the northwestern quadrant (B), the southeastern quadrant (C), and the southwestern quadrant (D), relative to an observer (see Fig. 2 in

Ray & Hess 2008). A statistical study using the ground-based radio observations from the Nançay Decameter Array (Marques et al. 2017) established the distribution of each DAM type in the central meridian longitude (CML)-Io phase diagram.

In previous studies focusing on the DAM source location and emission characteristics, remote sensing observations combined with modeling were commonly used before the advent of in situ observations. For Io-DAM emission, Hess et al. (2010) fitted the Io-DAM arcs in the radio spectrum based on emission angle function and summarized an empirical relation between the resonant electron energy and Io's position in System III (SIII) longitude. The authors also regarded the lead angle between active field lines of Io-DAM sources and Io as a parameter that depends on the details of the Io-Jupiter interaction. On this basis, Lamy et al. (2022b) developed an updated lead angle model, combining the previous model with UV observations of Io auroral spots and multiview observations in order to trace the instantaneous source and to then get the beaming angle and related electron energy for 11 DAM arcs. For non-Io DAM emission, the latitudinal beaming and frequency-longitude maps based on remote sensing observations were also statistically studied by Imai et al. (2008, 2011, 2017a), Louis et al. (2021), and Zarka et al. (2021). In situ observations by Juno provided some new understandings of DAM source locations. Louis et al. (2019) studied the source location of 26 non-Io DAM emissions with a wide longitude coverage, which corresponds to the average extent of the main auroral oval. And the non-Io DAM sources were encountered on the same range of magnetic field lines as HOM and bKOM.

Recently, Wang et al. (2020) developed a new method inspired from Hess et al. (2008) to infer DAM source locations and emission characteristics based on remote radio dynamic spectra. Wang's method only needs the time and frequency information of the observed DAM arcs to derive the locations of all the possible source field lines, which is different from other methods. In this paper, we extend the previous work by applying the method of Wang et al. (2020) to joint radio observations acquired between 2008 and 2014 by multiple spacecraft, including Wind, STEREO-A, and STEREO-B, to trace the source locations of DAM emissions and obtain their statistical properties.

The paper is structured as follows: In Sect. 2, we introduce the selection and classification of DAM events and present the observational statistical results of the events. In Sect. 3, we briefly describe Wang's method and present representative examples in different types of DAM events to illustrate the method. In Sect. 4, we show the statistical results of the inferred source locations, emission angles, and associated electron energy of the DAM events. Last, in Sect. 5, we provide a summary and a discussion of our work.

2. Observations and DAM events

Combining data from the Wind and STEREO missions can provide stereoscopic observations of Jovian radio emissions. The Wind spacecraft was launched in November 1994 and is currently in a halo orbit around the L1 Lagrange point. It carries the WAVES instrument (Bougeret et al. 1995) for measuring plasma and radio waves in space. The instrument's radio receiver band 2 ranges from 1.075 MHz to 13.825 MHz, with a 50 kHz-frequency step. The STEREO mission consists of twin spacecraft, STEREO-A (ST-A) and STEREO-B (ST-B), launched in October 2006. The two spacecraft orbited the Sun

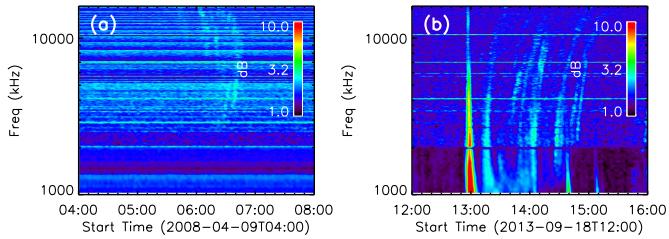

Fig. 1. Examples of excluded events with complex structures. Panel (a): ambiguous boundaries of the arcs. Panel (b): group of arcs with intervals at tens of minutes in the spectrum.

and respectively drifted about 22 degrees every year from the Earth in opposite directions (i.e., from 22° in 2008 to 163° in 2014). The STEREO/WAVES instrument (Bougeret et al. 2008) has high-frequency dual sweeping receiver (HFR), operated in the 0.125–16.075 MHz range. We used one minute averaged data (i.e., normalized receiver average voltage above the measurement background, in dB) from the Space Physics Data Facility (SPDF [1]). All the WAVES instruments cover the low-frequency band of DAM emissions; however, the higher frequency part of emissions is not covered.

2.1. Selection of events

Thanks to the stereoscopic observations from multiple spacecraft, DAM can be easily distinguished from solar radio burst due to the large time difference among the time-frequency spectra from the different spacecraft. The azimuthal separation between Wind, ST-A, and ST-B could be up to about 21° with respect to Jupiter. Thus, the time difference of observed DAM could be up to a few hours, mainly due to the rotation of the radio source along with Jupiter or its satellite, Io. Alternatively, with the known angular separation of the observers with respect to Jupiter, the rotational speed of the radio source of a DAM can be estimated by measuring the time difference between observations of the same DAM event by different observers. We manually checked the radio dynamic spectra from 2008 to September 2014, which is when ST-B lost communication, of the three WAVES instruments to select the DAM events. The selection criteria are as follows: (1) a selected DAM should be observed asynchronously by at least two spacecraft and should have similar morphology in a broad frequency range. Considering the limit of the thickness of the emission wall (Panchenko & Rucker 2016), the separation angle of the two observing spacecraft should be greater than 2° with respect to Jupiter. (2) Setting the intensity threshold at 1.05 dB above the background for Wind and 2 dB above the background for STEREO implies that we select intense DAM events. (3) The events are isolated and do not contain complex structures in the spectrum. Figure 1 shows two counter examples. Both consist of a set of arcs likely generated by multiple reflections of Alfvén waves between the Io plasma torus and Jupiter's ionosphere Gurnett & Goertz (1981). The presence of multiple groups of arcs makes it difficult to identify a clear association between two different spacecraft. Based on the above criteria, we selected 81 DAM events (see Table A.1), among which 62 events were observed by all three spacecraft. For the other 19 events observed clearly by only two spacecraft, the third spacecraft was not between the other two with respect to Jupiter to mostly guarantee the continuous emission of the DAM. Assuming the emission is continuous, we found that all

[1] https://spdf.gsfc.nasa.gov

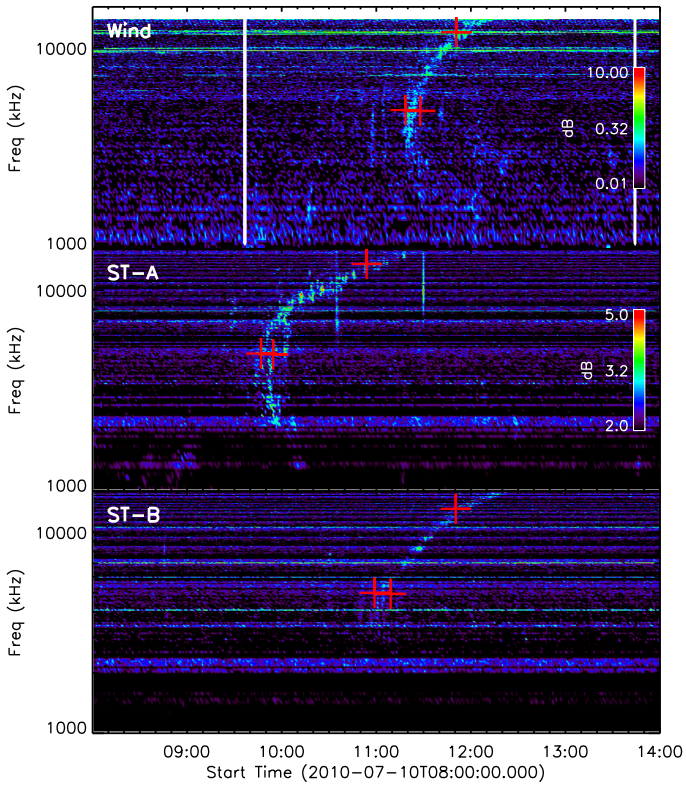

Fig. 2. Radio dynamic spectrum from Wind/WAVES, ST-A/WAVES, and ST-B/WAVES. The red markers indicate the start and end time at the apex of the arc and the start time of the leading end of the arc.

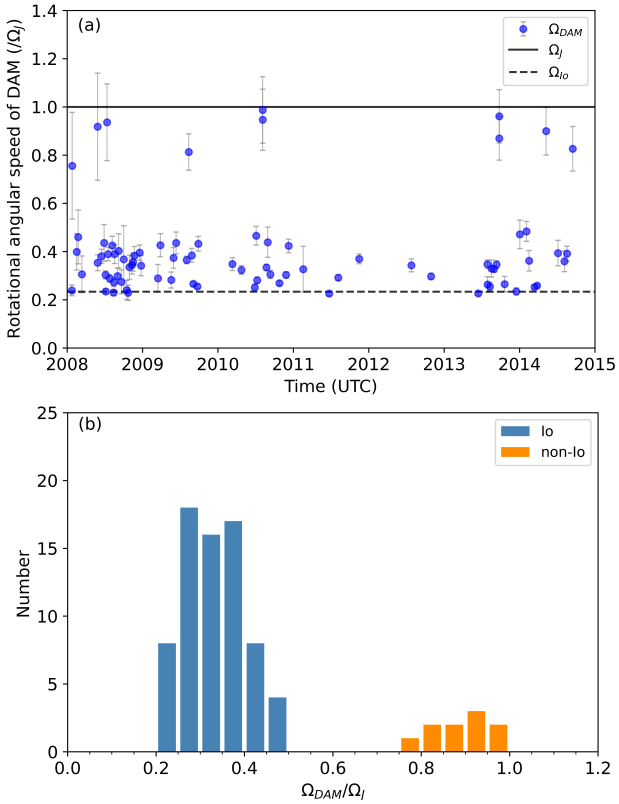

Fig. 3. Statistical rotational angular speed of DAM emissions. Panel (a): median values and error bars indicating the time uncertainty when considering ±4 min on the radio dynamic spectrum. The rotational angular speed of Io and Jupiter are represented by a dashed line and a solid line, respectively. Panel (b): histogram of the averaged rotational angular speed of DAM emissions in bins of 0.05 Ω_J. These events can be divided into Io-related (blue bars) and non-Io-related (orange bars) DAM emissions.

the selected events lasted for more than 30 min. Thus, our sample has a bias toward strong, long-lasting, and isolated DAM arcs.

2.2. Classification of DAM types

To distinguish between Io-DAM and non-Io DAM events, the apparent angular rotation speed, $\Omega_{\rm DAM}$, of a DAM emission was used. This value can be calculated by the angular separation, ϕ, between two spacecraft; the time difference of light travel, $\mathrm{d}t_l$, from Jupiter to the two spacecraft; and the time difference of the observed DAM features, $\mathrm{d}t = t_2 - t_1$, in which t_1 and t_2 are the times of the DAM in the radio dynamic spectra of the two spacecraft, respectively, that is,

$$\Omega_{\rm DAM} = \frac{\phi}{\mathrm{d}t - \mathrm{d}t_l}. \quad (1)$$

The main error source is the measure time t_1 and t_2. Since the time resolution of the used WAVES spectra is 1 min, the uncertainties in t_1 and t_2 are set to be $\Delta t_1 = \Delta t_2 = 2$ min. Thus, the uncertainty of the calculated $\Omega_{\rm DAM}$ can be estimated by the absolute error transfer formula as follows

$$\Delta\Omega_{\rm DAM} = \left|\frac{\partial\Omega_{\rm DAM}}{\partial t_1}\right|\Delta t_1 + \left|\frac{\partial\Omega_{\rm DAM}}{\partial t_2}\right|\Delta t_2 = \left|\frac{\phi}{(\mathrm{d}t - \mathrm{d}t_l)^2}\right|(\Delta t_1 + \Delta t_2). \quad (2)$$

For a DAM observed by all three spacecraft, we used the two spacecraft with the largest separation angle to derive $\Omega_{\rm DAM}$.

As an example, we show the DAM event observed on 2010 July 10 in Fig. 2. There is a VE arc in each spectrum from Wind/WAVES and ST-A and -B/WAVES. According to the apex of the arc marked by the leftmost red plus sign, the time delay, excluding light travel time, between Wind and ST-A is the longest, about 85.6 min. The angle between the two spacecraft with respect to Jupiter is about 14.44°. According to Eq. (1), the apparent rotation speed of DAM is calculated to be approximately $(0.281\pm0.013)\,\Omega_{\rm J}$, while the rotation speed of Io (Ω_{Io}) is about $0.23\,\Omega_{\rm J}$, in which $\Omega_{\rm J}$ is the rotation speed of Jupiter, it suggests that this DAM emission is an Io-related event. Figure 3a shows the apparent rotation speeds of the 81 events. The data points are mainly distributed between (and roughly around) Ω_{Io} and $\Omega_{\rm J}$. Figure 3b shows the histogram of the apparent rotation speeds. A double-peak distribution can be seen. One peak is located at around 0.25–0.3 Ω_J and the other around 0.9–0.95 $\Omega_{\rm J}$. This distribution suggests that the 71 DAM events around the first peak between 0.15 $\Omega_{\rm J}$ and 0.6 $\Omega_{\rm J}$ are Io-DAM emissions, and the ten events around the second peak between 0.7 $\Omega_{\rm J}$ and 1.2 $\Omega_{\rm J}$ are non-Io DAM emissions. Based on the rotation speeds, we may conclude that the occurrence probability of isolated, strong Io-DAM arcs is about seven times of that of isolated, strong non-Io DAM arcs. The reason for more Io-DAM events being selected is that the Io-DAM source is less extended spatially and less variable than the non-Io DAM source and thus more of these cases meet the selection criteria. In addition, Fig. 3b shows that the apparent rotation speed of Io-DAM events is typically greater than that of Io events, while non-Io DAM events generally rotate slower than Jupiter. We further classified the DAM emissions into A, B, C, and D types (e.g., Ray & Hess 2008). A DAM

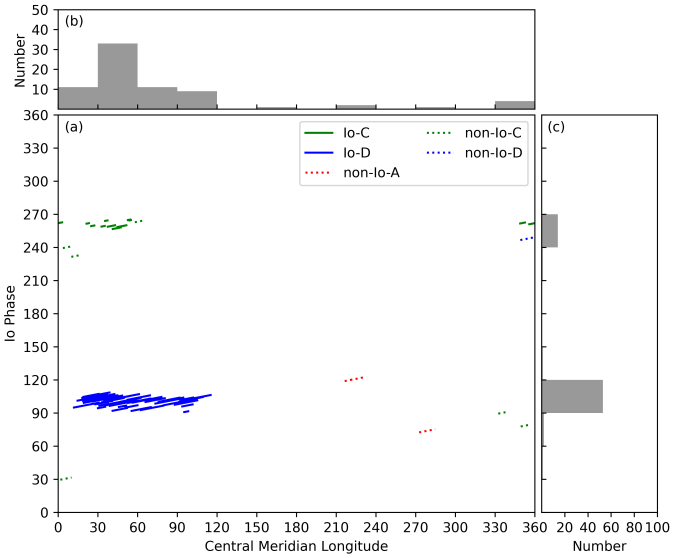

Fig. 4. Io phase versus west SIII longitude of Wind. Panel (a): CML and Io phase ranges over the entire Wind observation period of DAM emission. The solid line represents Io-DAM and the dash line indicates non-Io DAM. The color of lines represents the selected events in three source areas A, C and D. Panel (b): Histogram of CML in 30° bins. Panel (b): histogram of Io phase in 30° bins.

emission with a VE arc in the radio dynamic spectrum is from the western (B, D) hemisphere, while a DAM emission with a VL arc is from the eastern (A, C) hemisphere. However, it is hard to determine if a DAM emission originates in the northern (A, B) or southern (C, D) hemisphere without the polarization information. We determined from which hemisphere the emission is more likely to occur based on the occurrence of DAM events in the CML–Io phase plane (Marques et al. 2017). The four types of Io-DAM events occupy different regions in the plane of the observer's CML and the Io phase due to combined source location and beaming, though Io-A and Io-C (also Io-B and Io-D) have some overlaps in the CML–Io phase diagram. Similarly, all non-Io DAM event types occupy specific regions distributed in the CML. The difference, however, is that these events are uniformly distributed over the Io phase due to being Io independent. Also, we considered the tilt of the Jovian magnetic dipole axis. For instance, if the magnetic northern pole is toward the observer during a DAM emission, we considered it more likely that the DAM is from the northern hemisphere. Finally, we used the morphology of the t-f arcs based on Marques et al. (2017) to check the consistency of our identification.

According to the CML-Io phase diagram from Marques et al. (2017) obtained with ground-based observation, in Fig. 4 we display 74 of the 81 Io-DAM and non-Io DAM events observed by the Wind spacecraft close to the Earth in the CML–Io phase plane. The 74 events are in the regions where occurrence probability is above 10% (see Tables 4 and 5 in Marques et al. 2017) for each type. For these events, the CML is mainly distributed in 0°–180°, and the Io phase is concentrated in two intervals, one at 90°–120° and the second at 240°–270°. In the southern hemisphere, there are 12 Io-C events, 52 Io-D events, six non-Io-C events, and one non-Io-D event. In the northern hemisphere, there are only three non-Io-A events. Since the maximum radio frequency of DAM emission in the northern hemisphere is generally higher than those in the southern hemisphere (e.g., Genova & Aubier 1985; Hess et al. 2011; Marques et al. 2017). We note that being restricted to the low-frequency part of the northern emission arcs probably biases our selection. Thus, most of the identified events are from the southern hemisphere. In addition, we found that most non-Io events are distributed on the dusk side, which is consistent with previous results that found the fast-forward interplanetary shocks excite non-Io DAM emissions on the dusk side almost exclusively (Hess et al. 2012, 2014). The distribution of the identified events is also consistent with the results from Zarka et al. (2021), who found that HOM is related to non-Io DAM mostly coming from the dusk side. To balance the fact that the selected events are mostly distributed in the southern hemisphere, we randomly selected ten events located in the northern hemisphere from the database published by Marques et al. (2017) as a complement.[2] These events were observed by the Nançay Decameter Array (NDA; Boischot et al. 1980; Lamy et al. 2017, 2021; Lecacheux 2000) in the frequency range of 10–40 MHz. Among these ten events, five are Io-A and the others are Io-B. Similar to the previous selection criteria, the added events are strong and isolated arcs in the NDA radio dynamic spectra. The ten additional events are listed at the bottom of Table A.1.

3. Tracking the DAM source

3.1. Method

The method used to infer the DAM source is from Wang et al. (2020). The main idea is to use the properties of the observed DAM arcs to constrain the quadrant of Jupiter and search all the magnetic field lines from the quadrant to find source regions (or the active field lines) that satisfy the time-frequency drift pattern of the observed DAM arcs, which is described by the following function given in Hess et al. (2008):

$$\theta = \arccos\left(\frac{v}{Nc}\frac{1}{\sqrt{1-\frac{f}{f_{\mathrm{ce,max}}}}}\right), \tag{3}$$

where f is the observed frequency, approximated to the electron cyclotron frequency, and $f_{\mathrm{ce,max}}$ is the maximal electron cyclotron frequency at the active field line footprint (AFT). We set $f_{\mathrm{ce,max}}$ to be the value at 900 km altitude, as it corresponds to the typical altitude of Io UV footprint (Bonfond et al. 2009). To continue, v is the electron velocity, c is the light speed, and N is the refraction index, which we approximated to one due to strongly magnetized plasma (i.e., $f_{\mathrm{pe}}/f_{\mathrm{ce}} < 0.1$–$0.2$) in the Jovian magnetosphere (e.g., Bagenal 1994). We note that Eq. (3) is based on electron loss-cone driven CMI (e.g., Hess et al. 2008, 2010), which has been found to occur in the Jovian magnetosphere by Juno in situ observations (e.g., Louarn et al. 2017, 2018; Louis et al. 2020).

Based on previous studies, the following constraints were applied when we searched for the active field lines: (1) the cone wall thickness is less than 2°, (2) the emission angle ranges from 55° to 90°, and (3) the electron energy is above 0.2 keV. Jupiter's magnetic field was modeled by combining the internal magnetic field based on the "JRM33" model (Connerney et al. 2022) with an extended field based on the current sheet model from (Connerney et al. 2020). In addition, we used a geodesic polyhedron with 40962 vertices to trace magnetic field lines (see Fig. 2 in Wang et al. 2020). From the geodesic polyhedron, we could obtain a nearly uniform distribution of the field line footprints, which is important for the calculation of median values

[2] http://cdsarc.u-strasbg.fr/viz-bin/qcat?J/A+A/604/A17

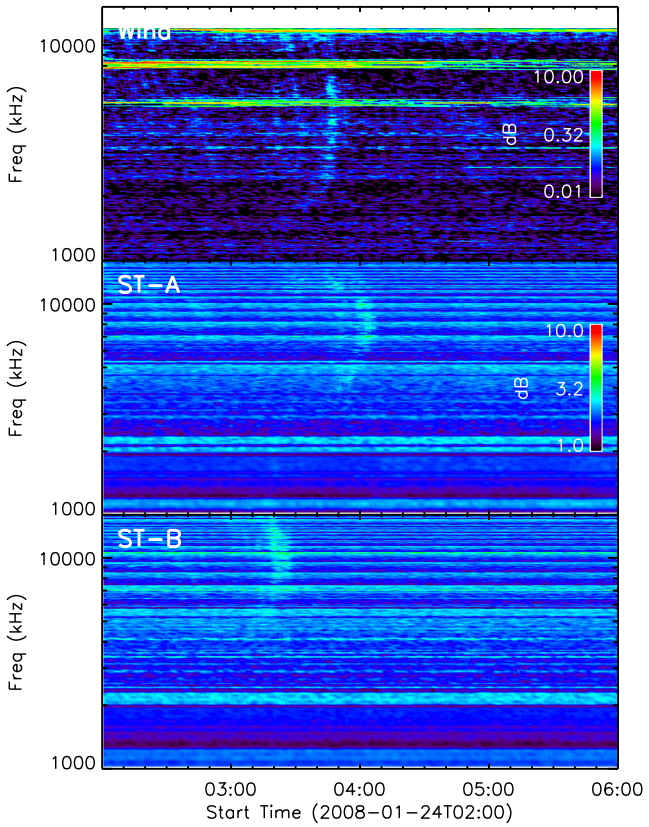

Fig. 5. Radio dynamic spectra of the Io-C emission on 2008 January 24 from Wind, ST-A, and ST-B.

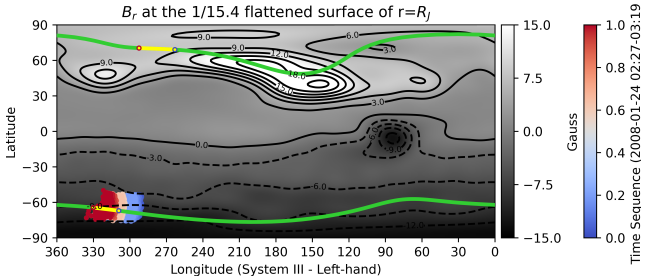

Fig. 6. Projected location of the Io-C emission at the flattened Jovian surface of 1 R_J. All modeled source footprints are shown as blue-to-red dots varying with observation time. The Io footprints are shown as green lines in the northern and southern hemispheres according to where the yellow segments represent the local Io footprints at observation time.

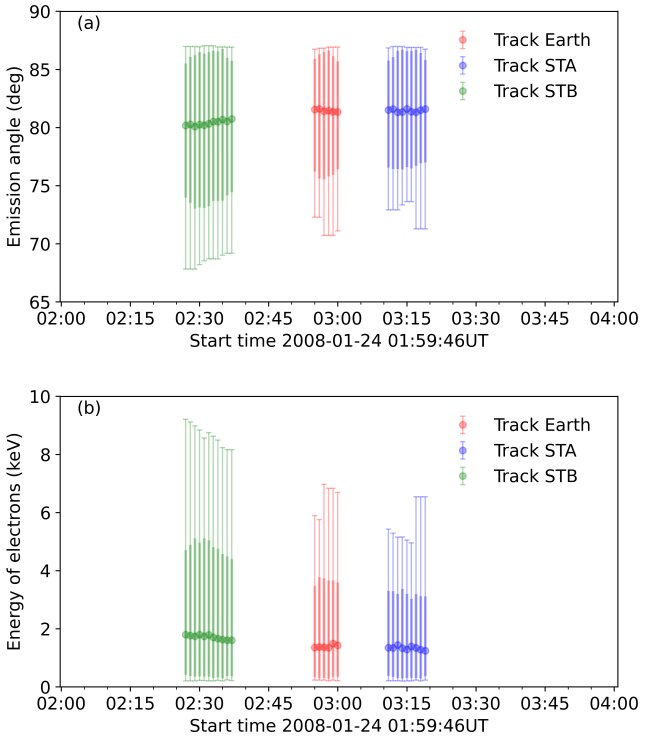

Fig. 7. Inferred emission parameters for the Io-C emission. Panel (a): emission angle. Panel(b): resonant electron energy. The circles give the median values, the thin bars give the minimum and maximum values, and the thick bars give the top and bottom tenth percentiles.

of derived parameters. The footprints are separated by approximately 1°, which meets the angular resolution required from the thickness of emission cone wall.

In the following subsections, we illustrate the method with three examples that belong to the above identified Io-C, non-Io-A, and non-Io-C types. One of the Io-D events has already been presented in Wang et al. (2022) and Lamy et al. (2022a).

3.2. Io-C event on 2008 January 24

An Io-C event was observed on 2008 January 24 by Wind, ST-A, and ST-B (see Fig. 5) from 02:27 to 03:19 UT, excluding light travel time. The portion of the arcs in the radio spectra from 5 to 9 MHz was selected to be used in our method. The snapshots of the source locations inferred from the three instruments are shown in the right panels of Fig. 5. The distance of the magnetic equatorial crossing of field lines (called M-shell value) ranges from 3.0 to 10.5 R_J, with a median of 5.1 R_J (Jovian equatorial radius $R_J = 71\,492$ km), which includes Io's orbit $\approx 5.95\,R_J$. To visualize the results, the footprints (FPs) of the active field lines on Jupiter's surface are shown in Fig. 6, and the Io auroral footprint (IFP) according to JRM33 (Connerney et al. 2022) is also plotted for comparison. The median longitude of the FPs drifts from about 299° to 320° with observational time, while the IFP in the southern hemisphere drifts from 306° to 328°, with a lead angle of about 7°–8°. The angular rotation speed of DAM emission in observed spectra is about $\Omega_{DAM} \approx (0.24 \pm 0.02)\,\Omega_J$. Similar to the calculation for the apparent angular rotation speed, the angular rotation speed of the FPs is about $\Omega_{FP} \approx (0.32 \pm 0.10)\,\Omega_J$ and that of the IFP is about $\Omega_{IFP} \approx 0.29\,\Omega_J$ in the inertial coordinates. Figure 7 illustrates the emission angle and the resonant electron energy during the multiview observations. The median emission angle has a small increase from 80° to 82°. This is probably what causes the apparent rotation speed Ω_{DAM} to be smaller than that of the FPs Ω_{FP}. Correspondingly, the median energy of active electrons decreases from 1.8 keV to 1.3 keV.

3.3. Non-Io-A event on 2010 August 6

A non-Io-A event was observed on 2010 August 6 from 02:07 to 03:00 UT when the observed radio wave was emitted from Jupiter. The located DAM source corresponding to the frequency range of 4–10 MHz is shown in Fig. 8, for which the inferred location is between 0.4 and 0.9 R_J above the Jovian surface and the M-shell value ranges from 6 to 14 R_J. The projected locations of the source and Io (see Fig. 9) show that the longitude range of

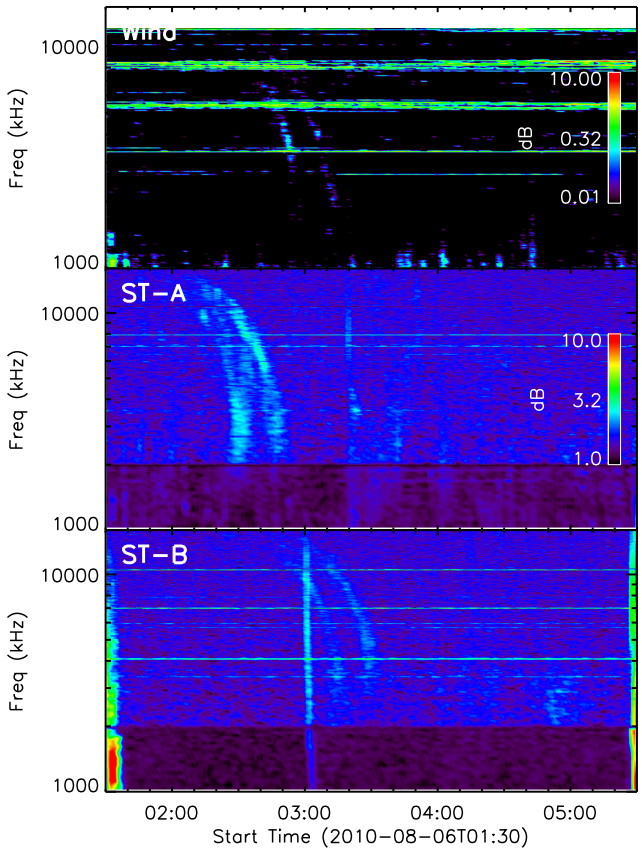

Fig. 8. Same as Fig. 5 but for the non-Io-A emission on 2010 August 6.

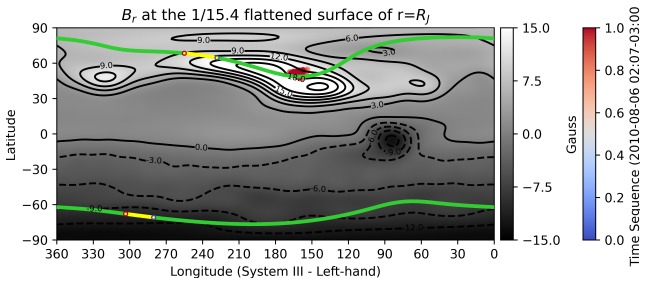

Fig. 9. Same as Fig. 6 but for the non-Io-A emission on 2010 August 6.

FPs is from about 158° to 165° and is separated from Io's footprint by more than 60° in longitude, confirming that the emission is unrelated to Io. The apparent rotation speed $\Omega_{\rm DAM}$ is about $(0.987 \pm 0.138)\ \Omega_{\rm J}$, and the rotation speed of the source footprint is $\Omega_{\rm FP} \approx (0.934 \pm 0.020)\ \Omega_{\rm J}$, where the median location of FPs in longitude drifts from 159.6° to 161.4°. The two speeds are quite consistent. The estimated emission angle (see Fig. 10) ranges from 55° to around 80°, with a quasi-steady median value of about 63°. Correspondingly, the median electron energy is about 16.5 keV and ranges from 5 to 25 keV, which is much higher than the Io-C event on 2008 January 24.

3.4. Non-Io-C event on 2009 August 13

A non-Io-C event was observed on 2009 August 13 from 01:50 to 03:00 UT (excluding light travel time), corresponding to the fit for the arcs in the frequency range of 6–11 MHz (see Fig. 11). The inferred source location is between 0.2 and 0.5 $R_{\rm J}$ above the Jovian surface, and the M-shell value ranges from 2.6 to 10

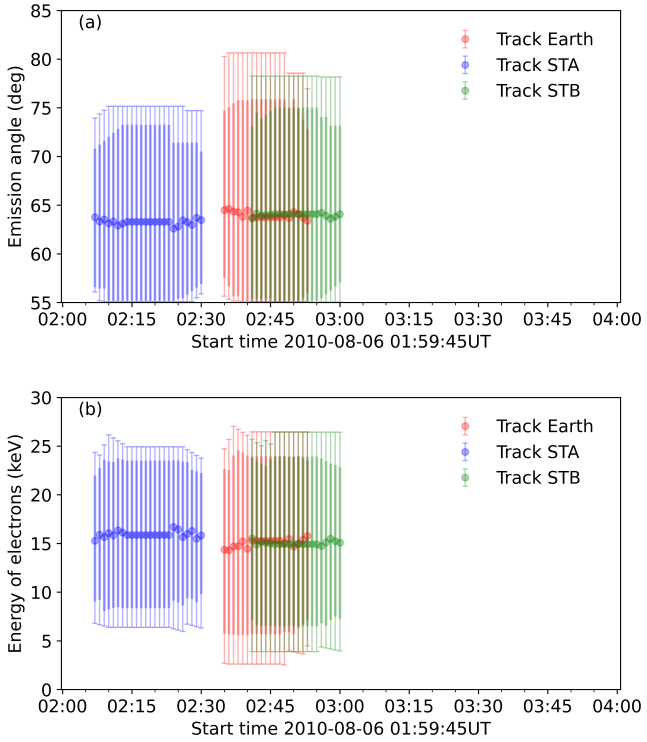

Fig. 10. Same as Fig. 7 but for the non-Io-A emission on 2010 August 6.

$R_{\rm J}$. According to all projected source locations in Fig. 12, the median FP in longitude drifts from 293.3° to 306.1°, which is close to the Io-C event on 2008 January 24 but far away from instantaneous Io's footprint. The apparent rotation speed $\Omega_{\rm DAM}$ is about $(0.813 \pm 0.075)\ \Omega_{\rm J}$, which is greater than the rotation speed of FP $\Omega_{\rm FP} \approx (0.70 \pm 0.01)\ \Omega_J$. The median emission angle in Fig. 13 has a slight decrease from 63° to 62°. Correspondingly, the median electron energy increases from 13.3 to 13.9 keV, which is higher than the Io-C event but lower than the non-Io-A event of August 2010.

4. Statistical results

In the 74 classified DAM events from multiview spacecraft observations, there are 69 DAM events for which we can find a source based on all spacecraft observations. The remaining DAM events were excluded from the following statistical analysis. The reason no source region was found for these five events is likely because they did not meet the constraint condition for electron energy in our model, which assumes that the energy of the electrons on a single field line is almost unchanged during the emission. When including the ten events from the NDA database, we have a total of 79 events with source information (70 Io-DAM events and nine non-Io DAM events). Their inferred properties are listed in Table A.2. These properties were obtained by combining all their observations. Figure 14 displays the footprints of active field lines with trajectory on the Jovian surface. The source locations of the DAM emissions are mainly concentrated in three regions, as shown in the histogram in Fig. 14. Two regions are in the southern hemisphere, between about 30° and 150° for Io-D and non-Io-D events and between about 270° and 330° for Io-C and non-Io-C events. The third region is in the northern hemisphere, between about 150° and 210° (non-Io-A, Io-A, and Io-B events). The latitudes of the three regions are mainly distributed around a latitude of ±60°, which

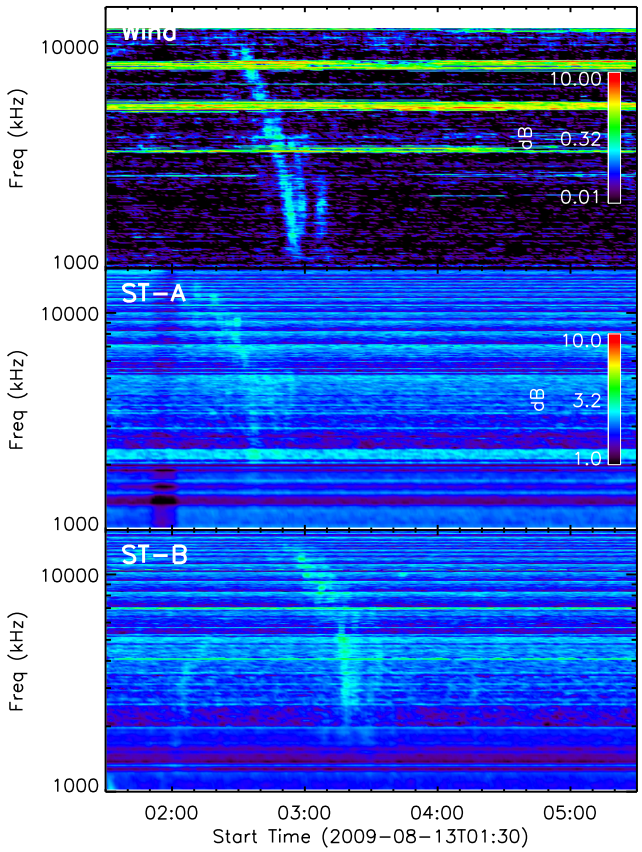

Fig. 11. Same as Fig. 5 but for the non-Io-C emission on 2009 August 13.

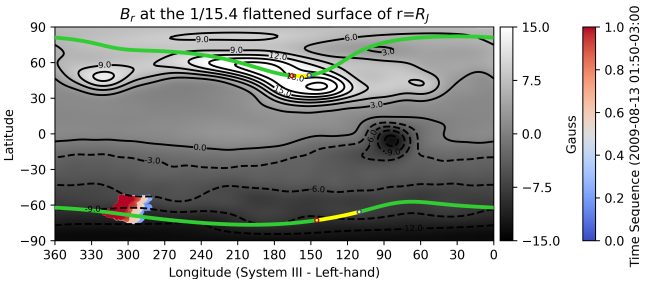

Fig. 12. Same as Fig. 6 but for the non-Io-C emission on 2009 August 13.

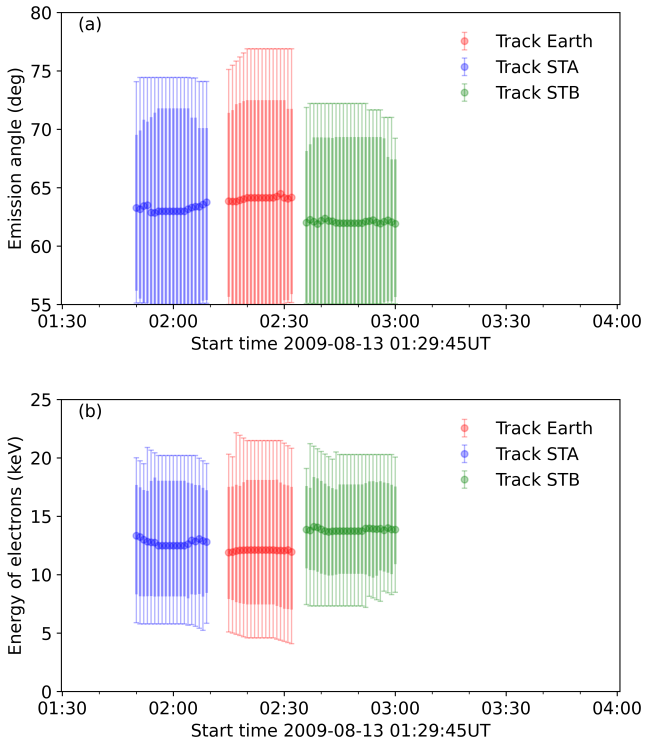

Fig. 13. Same as Fig. 7 but for the non-Io-C emission on 2009 August 13.

is near Io's footpath. In contrast to the CML–Io phase distribution studied previously, our study suggests that the actual source locations of A and B events in the northern hemisphere are concentrated around the strong magnetic anomaly, while the source locations of C and D events in the southern hemisphere are concentrated in two preferred longitude ranges, though the magnetic field strength has an almost uniform longitude at around 60° in the southern hemisphere. Each type of event has a specific preferred range of source regions. In the case of Io-DAM emission, two preferred ranges in the northern hemisphere around 160° to 170° and 177° to 192° correspond to Io-A and Io-B source regions, respectively. In the southern hemisphere, the Io-C source region is projected to be at 273° to 328°, while the Io-D source region is distributed from 50° to 122° in SIII longitudes. For non-Io DAM emission, we have limited statistics across eight dusk-side events (red triangles in Fig. 14) and one dawn-side event (yellow triangle). The non-Io-A source region is found from 161° to 186°, while the non-Io-C source region is located between 251° and 339° in SIII longitudes. The non-Io-D event is projected at 30°±5° longitude.

Different from remote sensing observations, Louis et al. (2019) analyzed the source locations of Jupiter's radio emissions in Juno's first 15 orbits by using in situ observations from Juno/Waves. The method to identify the source location involves comparing the local cyclotron frequency with the observed emission frequency. Their results show that the source locations of 26 non-Io DAM events had a wide longitude coverage along the auroral oval. This is different from our result, as we found that the source locations of our eight non-Io events are concentrated in their preferred regions in Fig. 14, which may be due to the bias in the event selection. The non-Io events selected in our study are of high radiation intensity and long duration (above 30 min) and are based on remote sensing observations, while the non-Io DAM events studied by Louis et al. (2019) have a shorter duration (2–3 min on average) and a narrower frequency band. Figure 15 shows the distribution of DAM source footprints on the Jovian surface in three dimensions. The colors of the source regions give the local time for when they generated DAM emissions. The dawn and dusk emissions are almost symmetrically distributed with respect to a certain longitude. In the southern hemisphere (Fig. 15b), this longitude is about 15°, and the dawn and the dusk emissions are located on the left and right sides, respectively, of the longitude line. It means that the region between 30°–150° not only prefers to generate DAM emissions but also prefers to emit during dawn, and the region between 270°–330° prefers to emit during dusk. In the northern hemisphere (Fig. 15a), the longitude around which the dawn and dusk emissions reversed is about 172°, though they are all concentrated in the magnetic anomaly.

The reason for this dawn-dusk symmetry as well as the preferred regions in southern hemisphere is not clear and is worth further investigation in future work. We think there might be

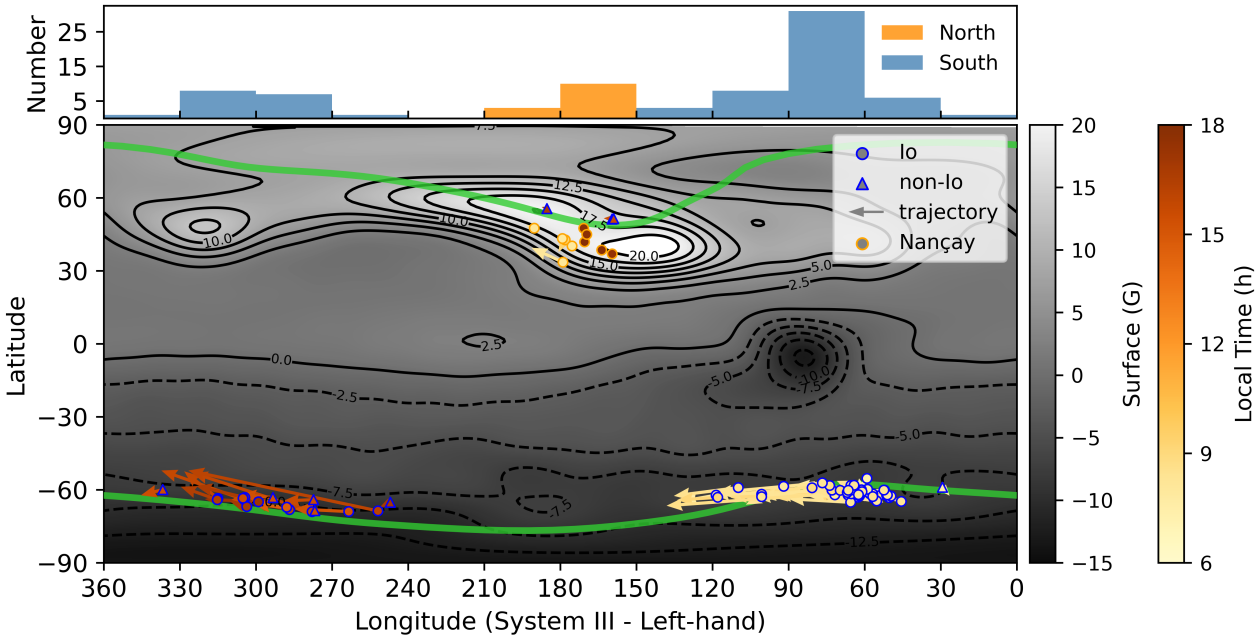

Fig. 14. Statistically projected location of the DAM sources in longitude and latitude. The dotted and triangular markers show the median locations of the starting footprints of active field lines for Io and non-Io events, respectively. The color-coded arrows indicate the trajectory of the footprints. The dots with orange edges represent the Io-related events observed by the NDA. The yellow-to-brown color bar indicates the local time of the source locations, reflecting whether the emissions are on the dawn or dusk side of the Sun's view. The histogram at the top indicates the distribution of longitude averages in the source region in 30° bins.

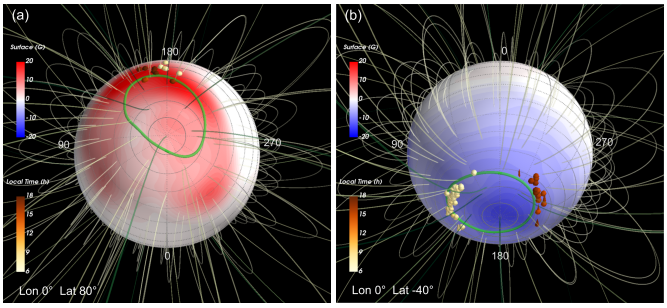

Fig. 15. Three-dimensional distribution of source footprints. Panel (a): distribution in the northern hemisphere. Panel (b): distribution in the southern hemisphere. The blue-to-red color on the ellipsoid surface of Jupiter shows the radial component of the magnetic field. Spherical and conical markers indicate the mean source footprints of the Io-DAM and non-Io DAM, respectively, and the color on the markers gives the local time. The green lines show the Io auroral footprints in the northern and southern hemispheres. The longitude and latitude shown in the lower-left corner of each panel indicate the position of Jupiter's disk center.

some singularities in the Jovian magnetospheric topology and/or the atmosphere or ionosphere around the pivotal longitudes. Moreover, there may also be sensitivity to the Sun-ward direction, from which solar radiation and solar wind interact with the Jovian system (including the magnetosphere, the ionosphere, Io plasma torus, etc). Related to this issue, Zarka et al. (2021) studied the non-Io DAM (auroral DAM) emissions and found that they are dominantly rotation-modulated where the rotational control is estimated to be three to four times stronger than solar wind control. The effect of solar activity on Io-DAM emission could be investigated in the future, but we note that Genova et al. (1987) found no effect for Io-dependent emissions.

The emission angle and corresponding electron energy for the DAM events were also inferred. Figures 16a and b show the

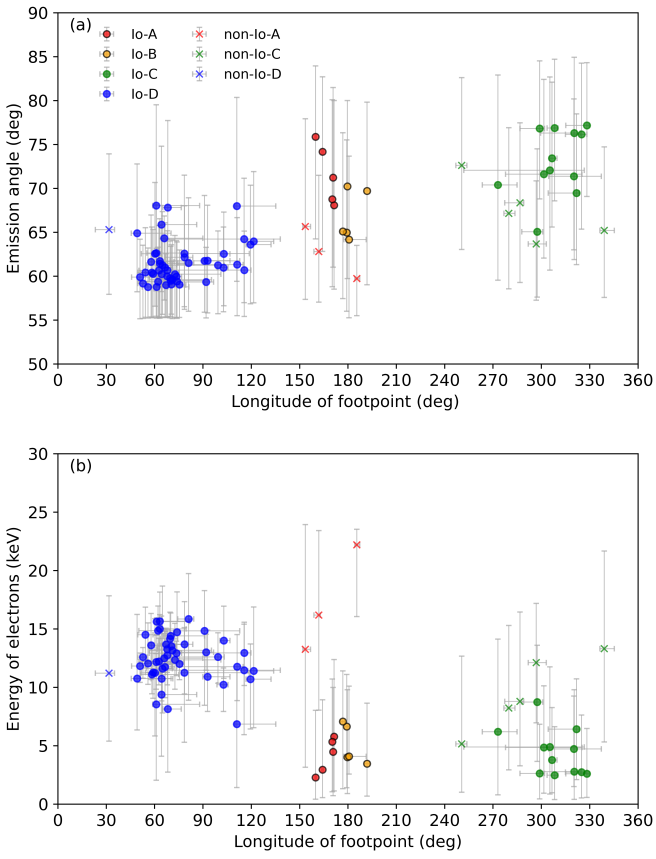

Fig. 16. Statistical emission parameters versus longitude of DAM source footprints. Panel (a): comparison for emission angle. Panel (b): comparison for active electron energy. The markers give the median values, and the gray bars give the top and bottom tenth percentiles. The dots with black contours in two panels represent the events observed by NDA.

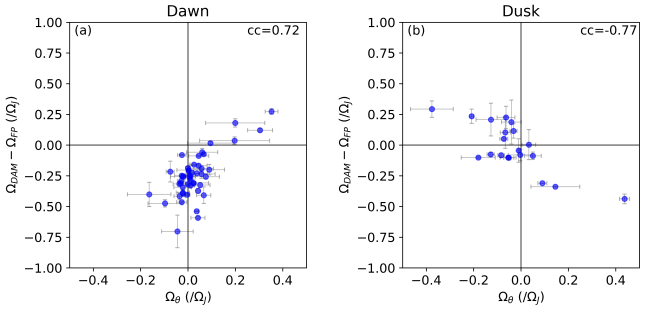

Fig. 17. Emission angle variation Ω_θ versus the difference in rotational angular speed between the apparent DAM arcs ($\Omega_{\rm DAM}$) and the source footprints for the emissions ($\Omega_{\rm FP}$) on the dawn side (a) and the dusk side (b). Emission angle variation $\Omega_\theta = \Delta\theta/\Delta t$ where $\Delta\theta$ means the overall change in the emission angle over the observation time Δt. The values were normalized by the rotational angular speed of Jupiter $\Omega_{\rm J}$.

median emission angle and resonant electron energy for all fitted events. The median emission angle for the Io-A events is distributed from 68° to 76°, which is larger than the range of 64° to 70° for Io-B events. The emission angle of Io-D is generally smaller, with the median value distributed between 60° and 68°, while the emission angle of Io-C is the largest, with the median value distributed between 65° and 81°. The non-Io events have smaller emission angles than the Io-DAM events of the same type. Correspondingly, the DAM electron energy is mainly distributed between 2 and 22 keV. The non-Io-A events have the largest electron energy, with the main range of 15 to 22 keV, and the Io-C, Io-A, and Io-B events have the smallest electron energy, with a range of 2 to 9 keV. The overall energy range is consistent with previous studies (e.g., Hess et al. 2010; Lamy et al. 2022b), but our statistical results reveal, for the first time, a systematic difference in the electron energy range between Io-related and non-Io DAM events. The electron energy of Io-A and Io-C is generally smaller than that of non-Io-A and non-Io-C, respectively. We note that since the uncertainties of these events are large, there are still overlaps. Furthermore, in the case discussed in Sect. 3.4, the apparent rotational angular speed differs from the rotational angular speed of the footprints. One possible cause of this difference is the evolution of the emission angle. For a DAM from the dusk side, when the emission angle increases, the apparent rotational speed observed from the remote radio instrument is smaller than the rotational speed of the footprints of the DAM source derived by our method. And if the emission comes from the dawn side, the apparent rotational speed is greater than that of the footprints with the increasing emission angle. To check if this behavior is true for all the events in our sample, we plotted the change of the emission angle $\Delta\theta$ versus the difference of the rotational speeds $\Delta\Omega$ between the end and start times for the 69 events based on the multipoint observations in Fig. 17. The result suggests a correlation between $\Omega_{\rm DAM} - \Omega_{\rm FP}$ and Ω_θ that supports a relation between the apparent rotation speed of the source and the evolution of the emission angle over the emission duration. The departure from a linear correlation may be due to the local magnetic field topology at the source location.

5. Summary and discussion

In this paper, we have presented a statistical study of DAM events based on multipoint observations with Wind and STEREO spacecraft. We selected 81 strong and long-lasting DAM events from 2008 to September 2014. Taking advantage of observations from multiple spacecraft, we estimated the apparent rotation speed in radio spectra and found that the apparent rotation speed could be used to distinguish Io-related and non-Io DAM events. The rotation speed of Io-DAM events is in the range of 0.15–0.6 $\Omega_{\rm J}$, and that of non-Io DAM events is between 0.7 and 1.2 $\Omega_{\rm J}$. Based on this criterion, the number of Io DAM events in the data is 71, and that of non-Io events is ten, suggesting that the occurrence probability of isolated, strong Io-DAM events is about seven times of that of isolated, strong non-Io DAM events. Based on CML–Io phase diagram from Marques et al. (2017) and the tilt of the Jovian magnetic dipole axis, we further identified 12 Io-C, 52 Io-D, three non-Io-A, six non-Io-C, and one non-Io-D. Due to the frequency coverage limitations of the radio instruments, the observations report many more DAM emission events from the southern hemisphere than from the northern hemisphere.

Further, we successfully inferred the source location, active field lines, emission angle, and resonant electron energy for 79 events (including ten NDA events) using the method by Wang et al. (2020). The ten NDA events were selected to supply sources from northern hemisphere (i.e., Io-A and Io-B emissions). The results from these NDA events help document the source region in the northern hemisphere and are consistent with the otherwise determined overall emission angle and the electron energy range. The distribution of different types of DAM source regions shows a clear north-south asymmetry, with one concentrated source region in the northern hemisphere around 150° to 210° (i.e., the magnetic anomaly) and two separate source regions in the southern hemisphere around 30° to 150° and 270° to 330°, respectively, in SIII longitudes projected onto the Jovian surface.

The preferred source regions for DAM emissions show a dawn-dusk symmetry in longitude (Fig. 15). In the southern hemisphere, the dawn and dusk emissions are almost symmetrically distributed with respect to the 15° longitude line. In the northern hemisphere, the pivotal longitude is about 172°, around which the dawn and dusk emissions are reversed. We believe this dawn-dusk symmetry may be related to some singularities in the Jovian magnetosphere and/or the ionosphere or atmosphere around the symmetrical longitude, which is worth further study in future work.

We also inferred different ranges of emission angle and resonant electron energy for different types of DAM emissions (Fig. 16). The electron energy range is between 2 and 22 keV for isolated, strong, and long-lasting DAM emissions, which is in good agreement with previous studies (e.g., Hess et al. 2010; Lamy et al. 2022b). Compared with Lamy et al. (2022b), the results of 11 events show that their inferred electron energy ranges from 3 to 16 keV, with a median value of 5.6 ± 2.7 keV and varies as a function of altitude and the Io's longitude (the latter's variation is shown in Fig. 16b). Our results regarding overall energy range are similar to those of Lamy et al. (2022b), especially for Io-B events, which are located at the same region in Io's longitude of 200°-250°. In addition, the energy in our results ranges up to higher values of 22 keV, specifically in non-Io-A emissions. Remarkably, the non-Io DAM events have a smaller emission angle and greater energy than Io-DAM events of the same type, especially for type A and C. The different emission characteristics between Io-DAM and non-Io DAM events may provide useful clues and constraints for further understanding of wave-particle interactions responsible for generating DAM emission. In our study, we also inferred the specific source region for each type (A, B, C, and D). In Table 3, we summarize the inferred parameters from this study and show the comparison with previous studies. The table shows that the properties of the source regions for Io-A, Io-B, Io-C and non-Io-A DAM events

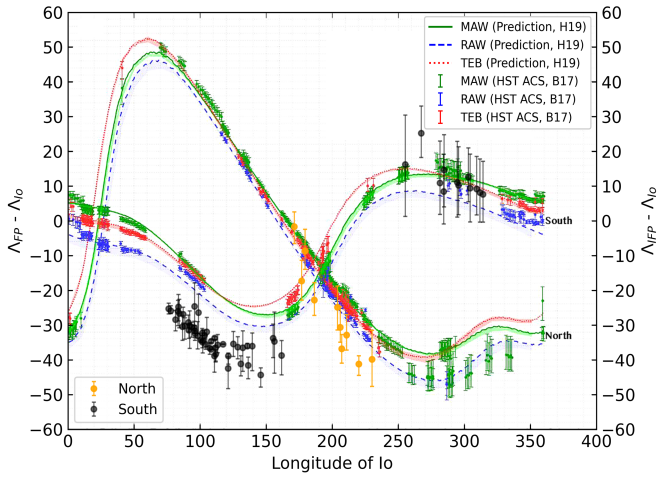

Fig. 18. Longitude difference between Io (Λ_{Io}), Io's auroral footprints (Λ_{IFP}), and Io-DAM source footprints (Λ_{FP}). The longitude difference between Io and the Io-DAM source footprints (orange and black dots) is shown on the left y-axis for comparison with the longitude difference between Io and Io's auroral footprints cited from Hinton et al. (2019), or H19, shown on the right y-axis. In H19, the locations of Io auroral spots were predicted for the main Alfvén wing (MAW), the reflected Alfvén wing (RAW), and the trans-hemispheric electron beam (TEB) for all longitude of Io with *Hubble* Space Telescope (HST) ACS observations (Bonfond et al. 2017, or B17).

are generally consistent across the various studies. However, we note that there is a systematic shift in our inferred source longitudes compared to previously observed and modeled Io auroral footprints (e.g., Bonfond et al. 2017, Hinton et al. 2019). As shown in Fig. 18, the longitude difference between our footprints of 70 Io-DAM events (Λ_{FP}) and of Io (Λ_{Io}) varies with the longitude of Io. For comparison, the longitude difference between Io's UV auroral footprints (Λ_{IFP}) and Io is superimposed in the right y-axis of the figure, and it shows the prediction based on the Alfvén wing model (H19) and observation by the *Hubble* Space Telescope (Bonfond et al. 2017, or B17). The source footprints of Io-DAM determined by our method vary with Io's longitude, following the same trend as Io's auroral UV footprints, as they both depend on the magnetic field topology of Jupiter and the Io-Jupiter interaction. Overall, the longitudes of the Io-DAM source footprints are relatively consistent with that of Io auroral UV footprints from the H19 model and B17 observation regarding the southern events in the range of 260°–320° and the northern events. However, for the events from the 70°–160° southern region, there is a systematic shift of about 15°. Since the shift is systematic and not randomly occurring for some individual events, it probably reflects the inaccuracy of our method for DAM events in some particular regions due to some unknown reasons, which could be the deviation from the assumed loss-cone driving mechanism of the CMI or in- and/or near-source refraction.

Acknowledgements. We acknowledge the use of the data from the radio instruments on board Wind, STEREO-A and B spacecraft. The authors thank the Nançay radio astronomy station/Nançay Scientific Unit of the Paris Observatory (USR 704-CNRS, supported by the University of Orleans, THE OSUC and the Centre Region in France) for providing access to NDA observations available online at https://www.obs-nancay.fr. The work is supported by the Strategic Priority Program of the Chinese Academy of Sciences (Grant No. XDB41000000) and the NSFC (Grant nos. 42188101, 42130204, 41974199 and 42174213). The work is also supported by the Informatization Plan of Chinese Academy of Sciences (Grant no. CAS-WX2021PY-0101). Y.W. is particularly grateful to the support of the Tencent Foundation.

References

Bagenal, F. 1994, J. Geophys. Res., 99, 11043
Boischot, A., Rosolen, C., Aubier, M. G., et al. 1980, Icarus, 43, 399
Bonfond, B., Grodent, D., Gérard, J. C., et al. 2009, J. Geophys. Res.: Space Phys., 114, A07224
Bonfond, B., Saur, J., Grodent, D., et al. 2017, J. Geophys. Res.: Space Phys., 122, 7985
Bougeret, J. L., Kaiser, M. L., Kellogg, P. J., et al. 1995, Space Sci. Rev., 71, 231
Bougeret, J. L., Goetz, K., Kaiser, M. L., et al. 2008, Space Sci. Rev., 136, 487
Burke, B. F., & Franklin, K. L. 1955, J. Geophys. Res., 60, 213
Carr, T. D., Desch, M. D., & Alexander, J. K. 1983, in Physics of the Jovian Magnetosphere (Cambridge University Press), 226
Connerney, J. E. P., Timmins, S., Herceg, M., & Joergensen, J. L. 2020, J. Geophys. Res.: Space Phys., 125, e28138
Connerney, J. E. P., Timmins, S., Oliversen, R. J., et al. 2022, J. Geophys. Res.: Planets, 127, e07055
Genova, F., & Aubier, M. G. 1985, A&A, 150, 139
Genova, F., Zarka, P., & Barrow, C. H. 1987, A&A, 182, 159
Gurnett, D. A., & Goertz, C. K. 1981, J. Geophys. Res., 86, 717
Hess, S., Cecconi, B., & Zarka, P. 2008, Geophys. Res. Lett., 35, L13107
Hess, S. L. G., Pétin, A., Zarka, P., Bonfond, B., & Cecconi, B. 2010, Planet. Space Sci., 58, 1188
Hess, S. L. G., Bonfond, B., Zarka, P., & Grodent, D. 2011, J. Geophys. Res.: Space Phys., 116, A05217
Hess, S. L. G., Echer, E., & Zarka, P. 2012, Planet. Space Sci., 70, 114
Hess, S. L. G., Echer, E., Zarka, P., Lamy, L., & Delamere, P. A. 2014, Planet. Space Sci., 99, 136
Hinton, P. C., Bagenal, F., & Bonfond, B. 2019, Geophys. Res. Lett., 46, 1242
Huff, R. L., Calvert, W., Craven, J. D., Frank, L. A., & Gurnett, D. A. 1988, J. Geophys. Res., 93, 11445
Imai, M., Imai, K., Higgins, C. A., & Thieman, J. R. 2008, Geophys. Res. Lett., 35, L17103
Imai, M., Imai, K., Higgins, C. A., & Thieman, J. R. 2011, J. Geophys. Res.: Space Phys., 116, A12233
Imai, M., Kurth, W. S., Hospodarsky, G. B., et al. 2017a, Geophys. Res. Lett., 44, 4584
Imai, M., Kurth, W. S., Hospodarsky, G. B., et al. 2017b, Geophys. Res. Lett., 44, 4455
Kaiser, M. L., Zarka, P., Kurth, W. S., Hospodarsky, G. B., & Gurnett, D. A. 2000, J. Geophys. Res., 105, 16053
Kurth, W. S., Gurnett, D. A., Clarke, J. T., et al. 2005, Nature, 433, 722
Lamy, L., Zarka, P., Cecconi, B., et al. 2017, in Planetary Radio Emissions VIII, 455
Lamy, L., Le Gall, A., Cecconi, B., et al. 2021, Nançay Decameter Array (NDA) Jupiter Routine observation data collection (Version 1.7) [Data set], PADC/CDN
Lamy, L., Cecconi, B., Aicardi, S., & Louis, C. K. 2022a, Earth Planet. Phys., 6, 10
Lamy, L., Colomban, L., Zarka, P., et al. 2022b, J. Geophys. Res.: Space Phys., 127, e30160
Lecacheux, A. 2000, Geophys. Monogr. Ser., 119, 321
Louarn, P., Allegrini, F., McComas, D. J., et al. 2017, Geophys. Res. Lett., 44, 4439
Louarn, P., Allegrini, F., McComas, D. J., et al. 2018, Geophys. Res. Lett., 45, 9408
Louis, C. K., Prangé, R., Lamy, L., et al. 2019, Geophys. Res. Lett., 46, 11,606
Louis, C. K., Louarn, P., Allegrini, F., Kurth, W. S., & Szalay, J. R. 2020, Geophys. Res. Lett., 47, e90021
Louis, C. K., Zarka, P., Dabidin, K., et al. 2021, J. Geophys. Res.: Space Phys., 126, e29435
Marques, M. S., Zarka, P., Echer, E., et al. 2017, A&A, 604, A17
Martos, Y. M., Imai, M., Connerney, J. E. P., Kotsiaros, S., & Kurth, W. S. 2020, J. Geophys. Res.: Planets, 125, e06415
Panchenko, M., & Rucker, H. O. 2016, A&A, 596, A18
Queinnec, J., & Zarka, P. 1998, J. Geophys. Res., 103, 26649
Ray, L. C., & Hess, S. 2008, J. Geophys. Res.: Space Phys., 113, A11218
Treumann, R. A. 2006, A&AR, 13, 229
Wang, Y., Jia, X., Wang, C., Wang, S., & Krupar, V. 2020, Earth Planet. Phys., 4, 95
Wang, Y., Zheng, R., Jia, X., et al. 2022, Earth Planet. Phys., 6, 13
Wu, C. S., & Lee, L. C. 1979, ApJ, 230, 621
Zarka, P. 1998, J. Geophys. Res., 103, 20159
Zarka, P., Queinnec, J., & Crary, F. J. 2001, Planet. Space Sci., 49, 1137
Zarka, P., Magalhães, F. P., Marques, M. S., et al. 2021, J. Geophys. Res.: Space Phys., 126, e29780

Appendix A: Tables

Table A.1. Statistics of emission parameters for observations.

No.	Date	Wind					Stereo-A					Stereo-B					VE/VL	Type	Rotation Speed
		Start time [UT]	Arc width [min]	Span time [min]	Start freq [kHz]	End freq [kHz]	Start time [UT]	Arc width [min]	Span time [min]	Start freq [kHz]	End freq [kHz]	Start time [UT]	Arc width [min]	Span time [min]	Start freq [kHz]	End freq [kHz]			
(1)	(2)	(3)	(4)	(5)	(6)	(7)	(8)	(9)	(10)	(11)	(12)	(13)	(14)	(15)	(16)	(17)	(18)	(19)	(20)
1*	2008-01-24	03:44:30	4	4	8880	11620	03:59:30	6	4	8320	11680	03:18:30	8	4	10120	13280	VL	Io-C	0.24
2	2008-01-25	18:24:54	4	12	4000	9940	18:27:38	5	14	3920	9800	18:16:58	6	10	3960	10240	VL	Non-Io-C	0.76
3*	2008-02-17	02:52:30	6	11	4920	7620	03:01:30	7	22	9620	13980	02:43:30	5	16	5820	8720	VE	Io-D	0.40
4*	2008-02-24	04:18:30	9	24	4780	9520	04:24:30	10	16	4920	8680	04:11:30	5	11	3920	8180	VE	Io-D	0.46
5*	2008-03-12	22:23:30	7	23	8320	12580	22:27:30	8	24	8880	13580	22:18:30	7	27	9570	13620	VE	Io-D	0.31
6*	2008-05-27	23:19:30	6	9	6820	12280	23:09:30	5	5	4780	10780	23:29:30	5	6	6080	11120	VL	Non-Io-C	0.92
7*	2008-05-28	00:38:30	8	27	8070	13280	00:07:30	7	32	7920	13320	00:50:30	13	21	7080	11920	VE	Io-D	0.35
8*	2008-06-16	10:41:30	11	31	4820	10180	10:29:30	12	37	9220	13820	11:09:30	10	17	4280	11120	VE	Io-D	0.38
9*	2008-06-28	20:28:30	8	22	7980	11280	-	-	-	-	-	20:47:30	7	21	5420	10120	VE	Io-D	0.44
10	2008-07-05	21:47:30	9	38	8180	12680	21:11:30	11	34	7780	13080	22:08:47	5	12	3900	8580	VE	Io-D	0.30
11*	2008-07-06	17:15:30	10	3	8820	13320	16:25:30	9	8	9520	14780	18:03:30	8	13	9430	14380	VL	Io-C	0.23
12*	2008-07-12	21:20:30	6	10	8520	13280	21:09:30	5	10	8720	13820	21:33:30	5	14	8820	14080	VL	Non-Io-C	0.94
13*	2008-07-18	07:00:30	8	23	7780	12120	06:41:30	9	28	9320	14180	07:41:30	10	37	9320	14520	VE	Io-D	0.39
14*	2008-07-26	03:46:30	7	4	8180	13620	03:19:30	7	3	8820	14780	04:28:59	9	1	9690	4000	VL	Io-C	0.29
15*	2008-08-06	17:39:30	6	21	6720	11620	17:16:55	9	29	4920	10430	17:57:30	8	26	8120	12880	VE	Io-D	0.42
16*	2008-08-13	18:43:30	8	18	5520	9320	18:40:30	8	24	7380	11980	19:48:00	5	13	4860	9630	VE	Io-D	0.23
17*	2008-08-14	14:37:30	7	9	8180	12880	14:20:30	7	7	8020	14420	15:16:30	8	14	8180	14380	VL	Io-C	0.27
18*	2008-08-19	03:07:30	9	24	8070	11180	03:01:30	8	14	7980	11720	03:29:30	7	19	5720	9680	VE	Io-D	0.39
19*	2008-09-02	05:45:30	7	28	7780	12680	05:45:30	7	14	6880	11480	06:14:30	7	26	8620	13920	VE	Io-D	0.30
20*	2008-09-07	13:58:30	9	27	9570	13520	14:05:30	8	37	10580	14780	14:20:30	8	32	9280	13980	VE	Io-D	0.40
21*	2008-09-20	18:27:30	6	6	8380	13220	18:38:30	6	7	7920	12780	18:40:30	8	12	9720	14680	VL	Io-C	0.27
22*	2008-10-02	09:06:30	8	19	9380	12280	09:14:30	9	29	8070	12720	09:04:30	8	34	8220	12980	VE	Io-D	0.37
23*	2008-10-16	12:36:30	7	16	9220	11720	13:06:23	6	17	6820	12550	12:41:30	9	27	11080	13620	VE	Io-D	0.24
24*	2008-10-22	15:02:30	7	12	10120	13280	15:38:30	8	13	10820	15920	-	-	-	-	-	VL	Io-C	0.23
25*	2008-10-29	17:13:30	5	2	8880	12080	17:36:30	7	7	8620	12820	16:59:30	7	4	7720	12820	VL	Io-C	0.34
26	2008-11-11	-	-	-	-	-	03:07:30	7	1	8430	11580	02:26:30	5	3	9120	12880	VL	Undefined	0.34
27*	2008-11-15	15:12:30	8	34	8780	13680	15:45:30	7	30	8620	13680	15:08:30	8	34	11320	14920	VE	Io-D	0.36
28*	2008-11-22	16:36:30	7	20	7020	10920	16:59:30	7	23	5580	10780	16:19:30	8	26	7920	12580	VE	Io-D	0.38
29*	2008-12-17	12:02:30	7	19	7220	10820	12:23:30	8	20	6080	9980	11:32:30	10	28	8680	12720	VE	Io-D	0.40
30*	2008-12-25	09:13:30	6	3	7320	11880	09:47:30	6	6	6280	12020	-	-	-	-	-	VL	Io-C	0.34
31*	2009-03-16	20:28:30	5	3	9620	13680	20:40:30	7	5	9020	14880	-	-	-	-	-	VL	Io-C	0.29
32*	2009-03-28	10:32:21	7	22	4910	11510	10:43:30	7	33	9780	14420	10:05:30	6	27	6680	10720	VE	Io-D	0.43
33*	2009-05-19	13:27:30	7	10	8020	12720	12:47:30	6	9	8020	14220	13:21:30	6	16	7980	13680	VL	Io-C	0.28
34*	2009-05-31	03:28:30	6	15	5120	10020	02:50:30	8	31	5820	11380	03:29:30	6	25	4780	11120	VE	Io-D	0.37
35*	2009-06-12	12:39:30	6	9	4380	9820	12:16:30	8	30	8620	14780	12:49:30	5	9	5720	10320	VE	Io-D	0.44
36*	2009-08-02	19:41:12	8	17	4030	10630	19:00:42	8	29	3960	13200	20:36:21	10	47	3900	9630	VE	Io-D	0.37
37*	2009-08-13	02:47:30	6	14	5680	11520	02:29:30	6	14	5880	11780	03:14:30	5	19	5420	11820	VL	Non-Io-C	0.81
38*	2009-08-27	14:26:30	11	33	7480	11980	-	-	-	-	-	15:19:30	7	29	6380	13720	VE	Io-D	0.38
39*	2009-09-03	15:36:30	10	33	7580	12620	15:15:30	8	31	7920	12920	17:01:30	13	45	4580	9320	VE	Io-D	0.27
40*	2009-09-23	21:46:30	7	4	8380	13780	21:38:30	8	12	8480	15620	23:11:01	11	25	6730	13800	VL	Io-C	0.26
41*	2009-09-28	10:36:30	7	23	8430	12320	10:48:30	8	26	11020	14620	11:20:30	8	40	5420	13420	VE	Io-D	0.43
42*	2010-03-12	02:13:30	7	28	7780	11680	03:01:30	10	28	7120	12280	01:22:30	9	29	10180	13620	VE	Io-D	0.35
43	2010-04-25	08:34:30	9	36	6620	11480	08:40:30	9	28	5720	11420	07:43:30	9	36	8220	12120	VE	Io-D	0.32
44*	2010-06-28	01:55:30	9	29	6420	10920	00:35:30	7	21	8430	11780	01:38:30	11	27	8520	12520	VE	Io-D	0.25
45*	2010-07-05	03:05:30	4	5	7220	12280	02:15:30	5	14	8380	13120	-	-	-	-	-	VE	Io-D	0.47
46*	2010-07-10	11:35:30	9	26	9380	13580	09:57:30	11	53	8020	13180	11:34:30	10	38	10720	15720	VE	Io-D	0.28
47*	2010-08-06	02:51:30	6	12	6280	10880	02:26:30	7	7	3120	7280	03:11:30	5	14	3620	9620	VL	Non-Io-A	0.95
48*	2010-08-06	03:03:30	5	17	7980	11520	02:38:30	6	14	5380	10180	03:24:30	6	16	5580	10980	VL	Non-Io-A	0.99
49	2010-08-23	-	-	-	-	-	15:41:30	10	40	10180	14520	17:07:30	10	24	5420	10220	VE	Undefined	0.33
50*	2010-08-30	18:39:30	10	29	7280	13620	16:35:02	6	42	4490	12800	19:13:30	10	13	4470	9680	VE	Io-D	0.44
51*	2010-09-12	03:39:30	9	24	7380	12380	02:29:30	10	36	8880	13180	-	-	-	-	-	VE	Io-D	0.30
52*	2010-10-26	08:39:30	9	25	8120	12180	08:37:30	9	22	7820	11420	10:28:30	11	34	6280	11680	VE	Io-D	0.27
53*	2010-11-27	04:49:30	7	17	8180	10920	05:17:30	8	25	6980	11120	06:06:30	7	26	4920	10180	VE	Io-D	0.30
54*	2010-12-09	14:21:30	8	22	8720	12520	14:54:30	8	32	6920	11220	15:12:30	7	6	4420	9120	VE	Io-D	0.42
55*	2011-02-18	09:32:30	7	23	4220	9320	-	-	-	-	-	09:09:30	7	21	4820	10020	VE	Io-D	0.33
56*	2011-06-24	03:33:30	7	14	4120	8570	02:44:30	12	26	5180	9430	01:59:30	8	19	6020	9820	VE	Io-D	0.23
57*	2011-08-07	09:36:30	9	26	8020	13280	07:48:30	7	22	6980	11720	09:08:30	10	44	9320	15280	VE	Io-D	0.29
58*	2011-11-16	05:25:30	10	29	6580	11080	-	-	-	-	-	06:49:30	10	31	5880	11180	VE	Io-D	0.37
59*	2012-07-26	09:14:30	7	11	5030	8020	08:15:30	9	40	7920	12420	-	-	-	-	-	VE	Io-D	0.34
60*	2012-10-29	22:34:30	11	33	8980	13180	20:59:30	9	32	7380	11380	22:39:30	10	32	9720	13380	VE	Io-D	0.30
61	2013-06-15	-	-	-	-	-	06:27:30	10	14	5480	9120	04:27:30	7	24	6280	10880	VE	Undefined	0.23
62*	2013-07-29	12:28:30	9	23	9720	12820	11:17:30	11	51	9120	12680	10:10:30	6	20	6680	10820	VE	Io-D	0.35
63*	2013-07-30	06:57:30	8	11	8520	12020	06:06:30	12	6	8980	14080	04:29:30	9	9	8280	12380	VL	Io-C	0.26
64*	2013-08-10	21:48:30	9	18	6580	9930	20:28:30	9	29	7220	11620	19:59:30	8	21	9180	12620	VE	Io-D	0.25
65	2013-08-17	-	-	-	-	-	22:17:30	9	40	8880	13880	21:42:30	9	38	8780	12980	VE	Undefined	0.33
66*	2013-08-30	08:39:30	7	13	7220	11520	07:27:30	10	39	7820	13920	06:56:30	7	15	7580	10780	VE	Io-D	0.33
67	2013-09-11	18:18:30	10	28	9320	13120	16:28:30	9	41	7380	12320	16:35:30	9	30	8320	11920	VE	Io-D	0.35

Table A.1. Continued from previous page.

68*	2013-09-24	21:13:30	5	18	4680	8680	20:33:30	9	17	4220	9070	20:44:30	8	14	3680	8380	VE	Non-Io-D	0.96
69*	2013-09-24	23:18:30	6	11	2520	6480	22:33:30	7	10	2380	7320	22:46:30	6	6	2380	5420	VL	Non-Io-C	0.87
70	2013-10-20	-	-	-	-	-	14:25:30	8	25	6880	12220	15:12:30	8	30	8220	13080	VE	Undefined	0.26
71	2013-12-16	-	-	-	-	-	06:35:30	9	34	8070	12720	07:16:30	9	24	4320	8520	VE	Undefined	0.23
72	2014-01-03	00:01:30	9	37	7820	12820	00:02:30	8	38	9620	14120	00:24:30	8	34	5580	11480	VE	Io-D	0.47
73*	2014-02-03	20:07:30	8	28	7920	13420	-	-	-	-	-	21:06:30	8	30	5820	11020	VE	Io-D	0.48
74	2014-02-16	-	-	-	-	-	06:27:30	7	32	6620	11820	06:50:30	8	16	4780	8520	VE	Undefined	0.36
75*	2014-03-14	17:17:30	7	24	4470	10580	19:25:30	10	26	5720	12320	19:44:30	8	16	5520	11480	VE	Io-D	0.25
76*	2014-03-27	03:03:30	9	30	7480	12080	04:12:22	8	21	4000	9150	05:27:30	10	47	7280	12280	VE	Io-D	0.26
77*	2014-05-10	06:07:30	7	20	6420	11280	06:32:30	7	25	8880	13580	06:20:30	11	19	9220	13420	VL	Non-Io-A	0.9
78*	2014-07-06	01:27:30	4	27	9570	13180	01:54:30	7	22	8070	11580	01:13:30	6	23	8020	11580	VE	Io-D	0.39
79*	2014-08-06	22:05:30	7	28	7680	12580	21:44:30	9	26	8280	12580	21:04:30	9	29	7220	12180	VE	Io-D	0.36
80*	2014-08-19	07:46:30	7	24	8120	11380	06:56:30	10	34	7380	12480	06:40:30	9	25	9620	13220	VE	Io-D	0.39
81*	2014-09-15	13:57:30	4	12	6320	11420	-	-	-	-	-	13:14:30	6	8	3620	9820	VL	Non-Io-C	0.83
NDA events																			
82*	2008-03-02	07:54:00	8	20	21000	31400	-	-	-	-	-	-	-	-	-	-	VL	Io-B	-
83*	2008-08-20	22:24:00	4	9	24000	31600	-	-	-	-	-	-	-	-	-	-	VL	Io-B	-
84*	2008-10-23	15:00:00	8	14	22000	30000	-	-	-	-	-	-	-	-	-	-	VL	Io-B	-
85*	2008-10-30	16:15:00	7	10	27000	34000	-	-	-	-	-	-	-	-	-	-	VL	Io-B	-
86*	2009-08-24	00:37:00	24	30	22700	33000	-	-	-	-	-	-	-	-	-	-	VL	Io-B	-
87*	2008-06-10	02:41:00	4	5	21500	30000	-	-	-	-	-	-	-	-	-	-	VE	Io-A	-
88*	2009-05-30	03:46:00	5	16	18000	28000	-	-	-	-	-	-	-	-	-	-	VE	Io-A	-
89*	2010-06-02	05:47:00	5	7	20000	30000	-	-	-	-	-	-	-	-	-	-	VE	Io-A	-
90*	2010-07-11	03:02:00	4	12	18700	31000	-	-	-	-	-	-	-	-	-	-	VE	Io-A	-
91*	2010-08-03	06:38:00	6	15	20000	31000	-	-	-	-	-	-	-	-	-	-	VE	Io-A	-

Column (1) lists the number of events. The asterisk indicates that the source location of the event can be inferred by our method. The events with numbers 83 to 92 were observed by the NDA. Column (2) presents the observed time in year-month-day format. Column (3) shows the first observed moment at the marker of DAM arc from the corresponding observer. Column (4) lists the observed period at the frequency of starting time. Column (5) indicates the time span from the moment corresponding to the start frequency to the moment at the end frequency regarding the frontier of the arc. Column (6) presents the start frequency, and Column (7) shows the end frequency. Columns (8)-(17) present the same information as Columns (3)-(7). Column (18) indicates whether the emission is composed of the VE or VL arc. Column (19) lists the types for DAM events. Column (20) shows the apparent rotation speed calculated with Eq. 1 based on multiview observations.

Table A.2. Statistics of emission parameters for our method.

No.	Longitude of Footprint [°]		Latitude of Footprint [°]		Emission Angle [°]			Energy of Electron [keV]		
	10%	90%	10%	90%	Avg	Med	Std	Avg	Med	Std
1	326.5	294.6	-75.2	-53.4	80.7	81.0	3.9	1.9	1.5	1.6
3	75.5	50.2	-65.5	-46.7	61.6	61.3	4.2	12.5	11.6	4.2
4	87.9	68.9	-65.8	-50.8	62.1	61.5	4.7	15.0	15.9	4.1
5	71.8	50.3	-64.8	-45.7	60.6	60.3	3.6	11.1	11.3	1.7
6	274.4	233.8	-77.2	-56.3	72.6	72.6	7.3	6.1	5.2	4.6
7	74.1	47.6	-64.1	-46.7	60.8	60.7	3.8	12.2	12.2	1.6
8	74.3	43.2	-66.1	-48.5	65.2	64.9	5.4	11.0	10.8	3.7
9	62.0	48.1	-65.8	-57.0	60.5	60.4	3.5	14.4	14.5	2.0
11	329.7	264.2	-75.3	-49.4	71.9	71.6	7.4	5.3	4.9	3.5
12	298.1	255.4	-75.6	-55.7	67.5	67.2	6.8	8.7	8.2	4.5
13	74.7	48.1	-64.6	-56.9	60.6	60.4	3.6	11.5	11.1	1.7
14	316.2	277.3	-75.2	-56.2	76.7	76.8	5.8	3.2	2.6	2.5
15	77.2	60.2	-63.9	-48.4	60.6	60.7	3.5	12.7	12.7	1.7
16	80.1	65.1	-64.1	-51.0	59.6	59.4	3.1	15.0	14.7	2.4
17	352.2	298.7	-73.3	-47.1	71.5	71.4	6.5	5.2	4.7	3.2
18	69.4	50.3	-65.0	-46.7	63.2	62.6	5.1	11.0	11.2	3.8
19	108.6	90.0	-65.0	-58.1	62.0	61.8	4.4	11.2	10.9	2.7
20	77.9	62.6	-62.5	-59.9	59.1	59.0	2.9	11.9	12.0	0.9
21	295.3	247.9	-76.1	-55.7	70.9	70.4	8.5	6.8	6.2	5.0
22	56.8	49.6	-64.4	-58.7	59.4	59.2	2.9	12.3	12.6	1.0
23	136.3	114.5	-71.3	-55.7	63.8	63.6	5.0	10.4	10.7	2.8
24	312.1	282.9	-74.3	-59.9	65.6	65.1	6.3	8.6	8.7	3.7
25	337.6	305.6	-72.1	-45.9	75.4	76.2	7.0	3.5	2.7	2.7
27	61.5	46.3	-64.1	-60.3	59.9	59.9	3.3	11.8	11.8	0.9
28	77.0	61.5	-64.1	-47.5	59.9	59.8	3.2	14.2	14.2	1.7
29	69.3	49.6	-65.0	-52.3	59.6	59.4	2.9	14.6	14.9	1.7
30	350.8	306.8	-74.4	-45.9	76.8	77.2	5.8	3.3	2.6	2.7
31	328.3	293.1	-74.1	-55.0	76.8	76.9	5.9	3.0	2.5	2.4
32	74.7	54.8	-65.3	-55.8	61.6	61.6	4.1	13.4	13.6	2.0
33	331.3	297.7	-73.3	-49.9	69.7	69.5	6.4	6.4	6.4	3.3
34	83.2	66.1	-65.1	-56.7	62.2	62.1	4.2	13.5	13.7	3.0
35	83.1	60.2	-65.2	-46.7	68.4	67.8	6.7	7.5	8.1	3.4
36	93.5	62.6	-63.1	-51.6	66.2	65.9	6.1	9.7	9.4	4.5
37	316.6	286.3	-73.3	-53.8	63.0	62.7	4.7	13.1	13.1	3.6
38	79.8	55.0	-65.8	-57.2	62.5	62.6	4.4	12.1	12.2	1.6
39	73.3	61.8	-62.9	-61.2	59.5	59.1	2.9	13.2	13.5	0.9
40	325.9	293.4	-74.2	-54.2	73.6	73.4	6.1	4.3	3.8	2.7
41	71.4	56.0	-64.9	-47.7	60.3	60.2	3.2	11.2	10.7	1.9
42	97.2	56.9	-63.1	-60.4	59.6	59.6	3.2	13.1	13.2	1.1
44	98.6	70.4	-63.6	-56.5	59.4	59.3	2.8	13.0	13.0	1.2
45	145.4	96.0	-70.5	-49.3	68.8	68.0	7.7	6.6	6.8	3.6
46	105.6	98.2	-63.8	-60.0	61.0	61.0	3.5	10.0	10.2	1.2
47	166.3	155.5	47.8	54.4	64.5	63.9	5.9	15.4	15.3	6.3
48	165.6	156.4	48.8	53.7	63.4	62.8	5.4	15.9	16.2	5.8
50	139.5	114.5	-70.1	-56.8	64.3	64.0	5.7	11.6	11.4	3.9
51	90.0	65.5	-65.2	-60.9	62.7	64.3	3.5	13.1	12.5	1.0
52	73.5	60.2	-63.1	-57.2	60.0	60.0	3.0	13.1	13.3	1.4
53	92.1	61.8	-63.5	-53.6	59.5	59.5	2.8	14.3	14.4	1.6
54	93.6	52.4	-65.1	-45.7	68.6	68.0	7.9	7.8	8.5	4.0
55	108.5	97.4	-67.5	-60.4	62.4	62.5	3.8	14.1	14.0	2.5
56	114.6	66.4	-68.2	-54.3	62.3	61.8	4.7	14.2	14.8	3.6
57	116.4	69.6	-65.2	-50.9	61.4	61.3	3.9	11.7	11.8	2.0
58	81.3	60.2	-62.7	-60.0	59.4	58.8	2.7	15.4	15.6	0.6
59	80.3	63.3	-63.6	-59.2	61.1	61.4	3.8	14.5	15.0	1.8
60	103.3	64.7	-64.2	-60.5	61.1	61.3	3.4	12.5	12.6	1.4
62	121.0	60.2	-64.2	-50.5	60.6	60.7	3.3	12.9	12.9	1.9
63	331.4	242.7	-74.2	-48.8	71.9	72.1	7.9	5.7	4.9	4.2
64	101.5	61.2	-64.5	-50.2	60.2	60.2	3.3	12.5	12.4	2.1
66	124.7	68.2	-68.5	-50.1	63.3	62.6	5.4	10.9	11.2	3.5
68	44.9	11.6	-70.8	-44.0	65.6	65.3	6.0	11.5	11.2	4.6
69	355.6	328.3	-73.5	-48.1	65.8	65.2	6.4	13.4	13.3	6.1
73	71.4	59.1	-64.2	-53.8	61.2	61.0	3.9	11.6	11.7	2.0
75	134.2	63.6	-69.2	-53.4	64.3	64.2	5.2	11.1	11.5	3.5
76	84.2	61.4	-66.1	-57.4	61.6	61.7	3.9	15.2	15.7	2.4
77	188.3	184.3	55.5	56.5	59.8	59.7	2.7	20.5	22.2	2.7

Table A.2. Continued from previous page.

78	80.6	62.8	-63.1	-57.8	59.2	59.0	2.6	13.6	13.7	1.2
79	78.3	56.7	-64.6	-57.1	60.1	60.0	3.2	12.7	12.9	1.1
80	68.5	51.2	-62.4	-57.5	59.1	58.8	2.9	12.4	12.0	1.8
81	303.9	269.9	-74.8	-54.1	68.5	68.4	6.8	9.3	8.8	4.9
82	190.8	170.0	32.4	53.9	65.7	65.0	7.2	6.5	6.6	3.5
83	190.2	169.0	31.7	57.2	70.0	70.2	7.6	4.8	4.0	3.3
84	187.4	165.9	30.3	56.4	66.1	65.1	7.1	6.7	7.1	3.6
85	209.1	176.3	37.9	59.8	69.6	69.7	7.7	4.1	3.5	2.9
86	191.3	174.4	32.4	51.3	63.5	64.2	6.7	5.6	4.1	3.2
87	171.2	152.2	24.4	51.9	75.0	75.9	7.2	3.3	2.3	3.0
88	182.0	161.4	24.2	53.9	68.7	68.1	7.7	6.4	5.8	4.2
89	172.3	156.7	24.7	53.4	73.4	74.2	7.3	3.9	3.0	3.2
90	177.5	163.6	25.5	53.8	71.2	71.2	7.6	4.9	4.5	3.4
91	179.1	161.5	24.9	53.9	69.2	68.8	7.8	5.7	5.3	3.6

The number of events is consistent with the number of events marked with an asterisk in Table A.1. The longitude and latitude of footprints are expressed as a range between the tenth and 90th percentiles.

Table A.3. Comparison with previous studies regarding source locations and resonant electron energy.

Reference	Type of events (number)	Source location [a] (°)	Energy (keV)
This work	Io-A (5)	160-170	2-6
	Io-B (5)	177-192	3-7
	Io-C (12)	273-328	2-9
	Io-D (48)	50 -122	7-16
	non-Io-A (3)	161-186	15-22
	non-Io-C (5)	251-339	5-13
	non-Io-D (1)	25-35	8-14
Lamy et al. (2022b)[b]	Io-A (2)	172-182 (1)	5-13
	Io-B(3)		2-6
	Io-C(2)		5-13
	Io-D(4)		4-16
Martos et al. (2020)[c]	Io-A (1)	177-180	10-15
	Io-B (1)	180-192	1.6-4.4
	Io-C (1)	295	11
Imai et al. (2017b)	A source (2)	163-183	0.5-11

[a] The projected source location in SIII longitude.
[b] One Io-A emission is represented by the main UV spot, and other events represented by Io's longitude are not listed here.
[c] The Io-D case in this paper is dubious and not listed here. We note that it has a more reasonable result in Lamy et al. (2022b).